

# Inhomogeneous Deformation and Texture Evolution of 30SiMn2MoVA Steel Gun Barrel Processed by Radial Forging Based on Cross-scale Crystal Plasticity Finite Element Method

Yuzhao Yang<sup>a\*</sup> , Cheng Xu<sup>a</sup>, Lixia Fan<sup>a</sup>

<sup>a</sup>Nanjing University of Science and Technology, School of Mechanical Engineering, 210094, Nanjing, China.

Received: March 10, 2022; Revised: June 28, 2022; Accepted: July 13, 2022

There is anisotropy in 30SiMn2MoVA steel gun barrel processed by radial forging which results in the low service life of the gun barrel. While the texture is the main reason for the anisotropy. The crystal plasticity finite element (CPFE) method is usually used to simulate the microstructure and the texture of the metal. In the present work, a two-dimensional polycrystalline finite element model based on electron back-scattered diffraction (EBSD) experiment data is developed to represent virtual grain structures of polycrystalline 30SiMn2MoVA steel. The displacement of nodes in the macro radial forging process finite element model is used as the cross-scale boundary condition in the CPFE model which realizes cross-scale simulation. The texture evolution and inhomogeneous deformation of 30SiMn2MoVA steel in the radial forging processing under three different forging ratios were simulated. The simulated texture results are consistent with the experimental results. The inhomogeneous deformation of grains is obvious and will intensify with the increase of the forging ratio. The distributions of stress and equivalent plastic strain in polycrystals are statistically Gaussian. With the increase of deformation, the further refinement of grains is due to the large shear strain in large grains.

**Keywords:** 30SiMn2MoVA steel, radial forging, cross-scale crystal plasticity finite element, inhomogeneous plastic deformation, texture.

## 1. Introduction

The 30SiMn2MoVA steel is a kind of high-cost performance die steel and has been used to produce gun barrels for many years in China. Radial forging, also known as rotary forging, is an open forging process used for reducing the diameters of shafts, tubes, stepped shafts and axels, and creating internal profiles for tubes such as rifling of gun barrels<sup>1</sup>. Radial forging is the mainstream process for producing gun barrel. During the process, the workpiece will stretch along the axis under the pressure of four high-speed hammers arranged radially around the primary tube. Previous studies have shown that the mechanical properties of the radial forged 30SiMn2MoVA steel gun barrel are anisotropic, and the transverse mechanical properties are worse than the axial mechanical properties, resulting in the low service life of the gun barrel<sup>2</sup>. The crystallographic texture is the main reason for anisotropy.

In order to improve the service life of the radial forged barrel, it is necessary to investigate the microstructure and texture of the radial forged gun barrel. The crystal plasticity finite element (CPFE) method has become an efficient tool to investigate the formation mechanism and the texture evolution during the plastic deformation of metals<sup>3</sup>. With the emergence of parallel computing, automatic data acquisition and advanced visualization tools, the finite element simulation of materials has gradually changed from macro simulation to multi-scale material simulation<sup>4</sup>. Peirce et al.<sup>5</sup> first used the crystal plasticity finite element method to simulate the tensile

deformation behavior of a single crystal in 1982. Due to the limitation of calculation conditions, they used the simplified setting of two symmetrical slip systems. Then Harren et al.<sup>6,7</sup> extended the model to polycrystalline. In 1991, Becker took the lead in simulating the 12 slip systems of face-centered cubic (FCC) crystals. He used the crystallographic degrees of freedom of the three-dimensional model to simulate the channel mold deformation process of cylindrical polycrystals and single crystals<sup>8,9</sup>. Since then, with the improvement of computing power, more and more scholars choose to use crystal plasticity finite element to study the characteristics of materials. In the micro field, they directly use the model of complex two-dimensional or three-dimensional grain arrangement with sub crystal scale grid<sup>10-14</sup> to study intergranular and grain internal force<sup>15,16</sup>, damage initiation<sup>17</sup>, interface mechanics<sup>18</sup>, and simulate micromechanical experiments (such as indentation, strut compression, beam bending) or predict local lattice curvature and mechanical size effect. In the macro aspect, in order to simulate the large-scale macro deformation process, a homogenized model has been developed<sup>19-21</sup>, which makes the CPFE model correctly represent the crystallographic texture in the statistical sense of the material. It can be applied to the large-scale forming process and texture evolution, including predicting the accurate material shape, thickness distribution, material failure, optimizing material flow, elastic springback, forming limit, texture evolution and mechanical properties after forming in the macro forming simulation<sup>22-24</sup>. Further, the CPFE can simulate the influence mechanism of surface morphology

\*e-mail: yangyuzhao@njust.edu.cn

involving macro (e.g. wrinkling) and microstructure (e.g. winding, wrinkling, orange peel)<sup>25</sup>. About the theory and application of crystal plasticity finite element, Roters et al.<sup>26</sup> made a detailed review. Crystal plasticity finite element has become an important research tool in the field of material processing. For the application of CPFE in radial forging, Xu et al.<sup>27</sup> established a two-dimensional polycrystalline finite element precision forging model with random shape according to the Voronoi method. However, his model did not consider the scale effect, and the grain size was much larger than the actual. The simulation results do not correspond well to the test results. Because the shape distribution and initial orientation of grains are not considered in their CPFE model.

In this work, a real 30SiMn2MoVA steel polycrystalline CPFE model was established based on EBSD experimental data. The geometric model contains real grain structure and crystal orientation. The shape function builds a bridge between the macro radial forging finite element model and the CPFE model. It makes the deformation displacement of the macro element as a cross-scale boundary condition added to the CPFE model. The texture evolution and grain deformation under three forging ratios were simulated. The simulated results were verified by EBSD experiments.

## 2. Materials and Methods

The chemical composition of 30SiMn2MoVA high strength steel is shown in Table 1.

Figure 1 illustrates the radial forging process. The workpiece flows axially under a large number of short-stroke and high-speed pressing operations by four hammer dies, arranged radially around the workpiece. When the hammer dies are raised, the workpiece will have the axial feed and rotational feed. The internal profile in a tube workpiece is created by the morphological characteristics of the mandrel. The type of radial forging machine is GFM SKK-10. The forging process is carried out at room temperature with coolant cooling. The strain rate is about 0.05–0.1/s. Three different forging ratios are 15%, 22% and 35%. The forging ratio,  $\eta$ , is also called the area reduction ratio, which is calculated by

$$\eta = \frac{(R_o^2 - R_i^2) - (R_1^2 - R_2^2)}{R_o^2 - R_i^2} \quad (1)$$

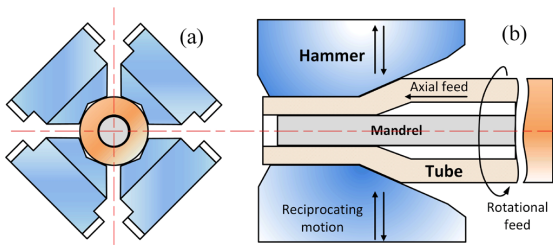


**Figure 1.** Schematic diagram of the radial forging process. (a) Layout of hammer dies; (b) Movement of workpieces and hammers.

**Table 1.** Chemical compositions of 30SiMn2MoVA steel(wt.%).

C	Si	Mn	Mo	V	P, S
0.27~0.33	0.90~1.20	2.20~2.60	0.30~0.40	0.05~0.12	<0.35

where  $R_o$  and  $R_i$  are the outer and inner radius of the tube blank and  $R_1$  and  $R_2$  are the outer and inner radius of the forged tube. The diameters of steel tubes are shown in Table 2.  $\eta$  equaling 0 indicates that the samples are made from the tube blank which is not forged.

Microstructural characterization of 30SiMn2MoVA steel tube blank and forged tubes was observed by a field emission scanning electron microscope (Oxford instruments) equipped with an electron backscatter diffraction (EBSD) system (AZtecHKL EBSD system). The measurement step size is 0.1 $\mu$ m used for the scanned area. The EBSD data of the 30SiMn2MoVA steel tube blank are used to establish the finite element geometric model of crystal plasticity. The EBSD data of forged materials are used to verify the results of finite element simulation.

## 3. Crystal Plasticity Finite Element Model

### 3.1. Crystal material model

The theory of crystal plastic deformation includes kinematics of crystalline deformation, crystal plastic constitutive relationship, and hardening model. The theories above have been developed very maturely and are widely used in the field of the crystal plasticity finite element, so they will not be introduced in detail in this paper. The finite element software ABAQUS(Version 6.13) is used to calculate the plastic deformation of crystals. The user-defined material subroutines (UMAT) in ABAQUS can realize the above crystal plastic deformation theory. The crystal plastic UMAT in this work is developed by Huang<sup>28</sup>. The material parameters in the crystal plastic UMAT include material elastic modulus matrix, slip system, initial grain orientation, hardening parameters, reference strain rate, strain rate sensitivity coefficient, iterative setting, and so on. Kovač et al.<sup>29</sup> considered that a small amount of alloy elements has little effect on the elastic modulus matrix of typical crystal materials. Therefore, in this study, the elastic modulus of 30SiMn2MoVA steel adopts body-centered cubic material  $\alpha$ -Fe is simplified instead. The body-centered cubic material has only three independent elastic variables, namely:  $C_{11}$ ,  $C_{12}$ , and  $C_{44}$ . According to the tensile experiment of 30SiMn2MoVA steel and the CPFE simulation of its tensile process, Xu et al.<sup>27</sup> fitted the relevant parameters required for the remaining CPFEM of 30SiMn2MoVA steel, as shown in Table 3.

30SiMn2MoVA is a body-centered cubic (BCC) material. There are 12  $\{110\} <111>$  slip systems, 12  $\{112\} <111>$  slip systems and 24  $\{123\} <111>$  slip systems, with a total of 48 slip systems. In this study, 48 slip systems are considered.

**Table 2.** The dimension of tubes under different area reduction ratios.

$\eta$ (%)	$R_o$ (mm)	$R_1$ (mm)	$R_2$ (mm)	$R_i$ (mm)
0	14	3.11	14	3.11
15	14	3.11	12.90	2.94
22	14	3.11	12.40	2.94
35	14	3.11	11.40	2.94

**Table 3.** Material parameters of 30SiMn2MoVA steel in crystal plasticity model.

elastic variable $C_{11}$ /(GPa)	elastic variable $C_{12}$ /(GPa)	elastic variable $C_{44}$ /(GPa)	Initial hardening modulus $h_0$ /(MPa)	Shear stress saturation value $\tau_s$ /(MPa)	Critical value of initial decomposition shear stress $\tau_d$ /(MPa)	Strain rate sensitivity coefficient $n$	Reference shear strain rate $\dot{\gamma}_0$ /(1/s)
230	130	117	300	220	175	10	0.001

### 3.2. Polycrystalline geometric model and mesh generation

In the study of the CPFEE of polycrystalline materials, the geometric modeling of polycrystalline materials is very important. The key to modeling is the characteristics of polycrystalline materials, such as grain shape, size, and distribution. At present, there are four common modeling methods. The first is to use regular polyhedrons such as tetrahedrons to represent the grain, which is quite different from the actual morphology of the grain and cannot reflect the real characteristics. The second is the cellular automata method, which is an algorithm to describe and deal with the evolution law of complex systems in discrete space and time. It is mainly used in the simulation of metal recrystallization and solidification. The third is the more popular Voronoi diagram method, which can generate the geometric characteristics and distribution of irregular grains. It is a common method to study the metal plasticity finite element. The polycrystalline model depends on the control parameters. The key to judging whether the model is available is to compare the polycrystalline model with the relevant material experimental results. In order to get close to the experimental results, the control parameters need to be adjusted continuously. The fourth is to obtain the crystal structure of the material through optical microscopy, such as the metallographic picture or EBSD maps, and redraw the experimental picture to construct its grain structure. This method can truly reflect the grain structure. In this paper, the fourth method will be used to construct a real two-dimensional polycrystalline geometric finite element based on the EBSD results of the 30SiMn2MoVA steel tube blank.

Analyzing the data form of EBSD, the generated material micromorphology picture is composed of a series of pixels, each pixel contains its position coordinates and the crystallographic orientation information of Euler angle, each grain is a set composed of multiple pixels, and the distance between adjacent pixels is equal to the scanning step of EBSD experiment. The idea of finite element is to divide the model into several small regular grids, and each grid is an element. This provides an idea for constructing the polycrystalline finite element model using EBSD experimental data. Each pixel of EBSD experimental results correspond to the element of the finite element model. The coordinate information of pixels is equivalent to the information of finite elements. Each grain is composed of several pixels. The cells converted from these pixels can be used to establish a cell set to represent the grains in the finite element model. The extracted cells, cell sets, and the crystallographic orientation (Euler angle) of pixels are written in the format of the ABAQUS source file "INP" file to complete the modeling of the polycrystalline finite element geometric model.

The extraction and writing of the above information into "INP" file are based on the open-source toolbox MTEX<sup>30</sup> of MATLAB software. The related modeling code is written with reference to the work of Iatypov<sup>31</sup> and Nicol<sup>32,33</sup>. Its functions mainly include three aspects. (1) Converting pixel type. Generally, most EBSD data pixels are hexagonal. However, most of the finite elements are quadrilateral or hexahedral meshes. To correspond the pixel information to the finite element mesh, the EBSD pixels need to be converted into quadrilateral pixels. This operation is based on "fill" function in the MTEX. "fill" function changes the values of phaseId and grainId from NaN to the value of its nearest neighbors. It can extrapolate spatial EBSD data by nearest neighbor for tetragonal lattice. (2) Cleaning up. EBSD experimental data usually contain some inaccurate pixels, which are not desirable to convert into the generated finite element model. These inaccurate pixels mainly include pixels with unrecognized phases, pixels with low confidence index (CI), and pixels belonging to too small grains. The implementation of this function depends on the "calcgrain" function in the MTEX. "calcgrain" function can realize the grain reconstruction. The grain reconstruction method is based on the definition of high angle grain boundaries. In the MTEX, grains are regions surrounded by grain boundaries. This function takes as input an EBSD data set and returns a list of grain. Each reconstructed grain contains phase, pixel number and orientation information. (3) Cropping and generating "INP" files. This part of the code is to sort out the required information generated by the "calcgrain" function, cut the EBSD data to the required size, and generate the "INP" file according to the format of the model data in the ABAQUS source file. The written information includes the unit converted by each pixel, the unit set representing different grains and the crystallographic orientation information of each grain.

The EBSD map of 30SiMn2MoVA steel tube blank is shown in Figure 2a. Figure 2b is the micromorphology after converting the pixel type and removing the inaccurate pixels. Import the generated "INP" file into the ABAQUS. The polycrystalline geometric finite element model established based on EBSD data is shown in Figure 3. The unit size of the model is equal to the EBSD scanning step size (0.1 $\mu$ m). The model includes 37829 elements, 996 element sets (number of grains), and 996 material properties. Each material property corresponds to a grain. The material properties contain the crystallographic orientation information of the grain.

### 3.3. Cross-scale boundary conditions

The cross-scale analysis is often used to solve the coupling between macro and meso. In order to make the meso model fully reflect the characteristics of the macro model, the shape and size of the meso model are the same as the important

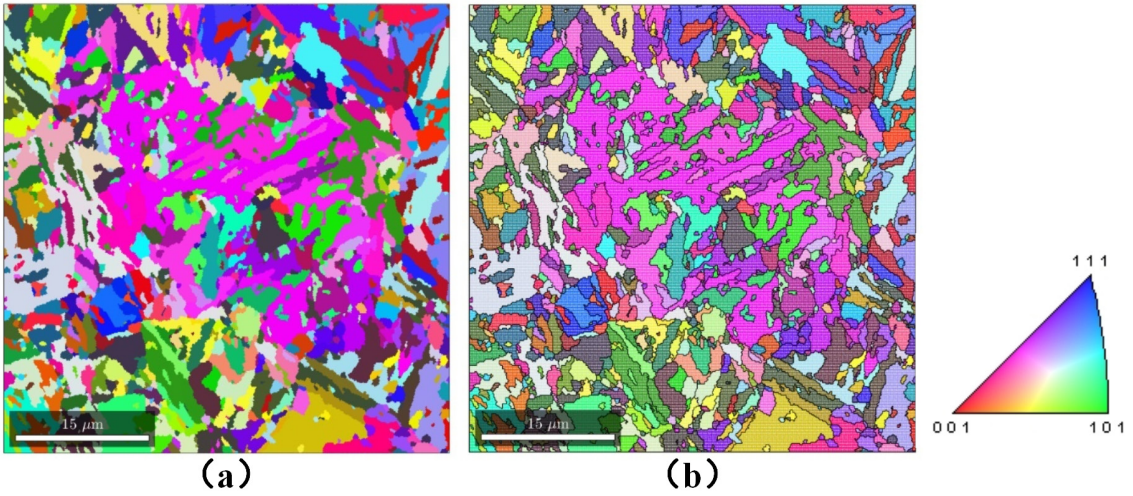


Figure 2 . EBSD diagram of 30SiMn2MoVA steel tube blank:(a) The original morphology obtained from the test; (b) Converted EBSD maps.



Figure 3. Polycrystalline geometric finite element model based on EBSD experimental data.

regions concerned in the macro model. then construct the shape function to interpolate the node displacement of the elements in the macro-region to obtain the new boundary conditions of the meso model.

The size relationship between the macro model and the meso is shown in Figure 4. The macro radial forging finite element model is used to obtain the deformation of steel barrels with different forging ratios. Its element size is 1mm. The local grid of the macro model is refined to make its element size 0.05mm. The refined grid element size is the same as the size of meso polycrystalline finite element geometric model. In order to make the boundary conditions of the meso polycrystalline material model fully reflect the surrounding stress field in the macro radial forging process, the displacement of four nodes of an element in the

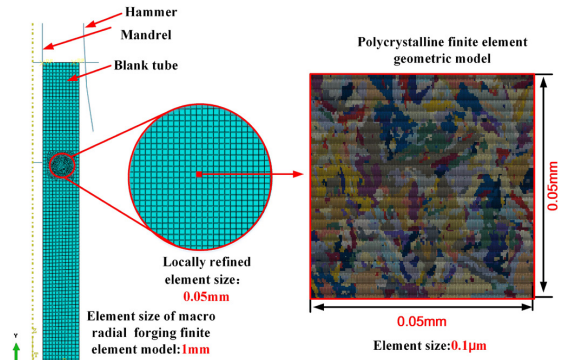


Figure 4. The dimensional relationship between macro radial forging finite element model and the CPFE model.

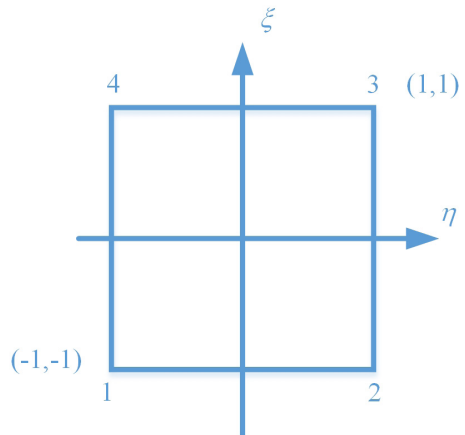


Figure 5. The four-node element.

calculation results of the macro radial forging finite element model under the three different forging ratio is extracted. Then according to the internal continuity theory, through

the shape function, the displacement of the extracted four nodes is interpolated to each node on the boundary of the meso polycrystalline finite element model.

The shape function can not only be used as the interpolation function of the element and represent the displacement of any point in the element with the node displacement but also as the weighting function in the weighted residual method. It can deal with the external load and equivalent the distributed force to the concentrated force and moment on the node. For the four-node element, in order to make the quartic polynomial in the interpolation function a complete polynomial, a node is established in the center of the element, and then the dimensionless local coordinates are introduced  $\xi$  and  $\eta$ , as shown in Figure 5,

Therefore, the local coordinates of any point can be expressed by the following formula:

$$\eta = 2 \frac{x - x_c}{x_n - x_1} = \frac{2x - (x_1 + x_n)}{x_n - x_1} \quad (2)$$

$$\xi = 2 \frac{y - y_c}{y_n - y_1} = \frac{2y - (y_1 + y_n)}{y_n - y_1} \quad (3)$$

$$x_c = (x_1 + x_n) / 2 \quad (4)$$

$$y_c = (y_1 + y_n) / 2 \quad (5)$$

Where  $x$  and  $y$  are the coordinates of any point,  $x_c$  and  $y_c$  are the coordinates of the cell center,  $n$  is the number of cell nodes,  $x_1$  and  $y_1$ ,  $x_n$  and  $y_n$  are the coordinates of node 1 and  $N$  respectively. The shape function of the four corner nodes of the element can be constructed by Lagrange polynomials, as shown in the following formula:

$$\begin{cases} N_1 = (1 - \eta)(1 - \xi) / 4 \\ N_2 = (1 + \eta)(1 - \xi) / 4 \\ N_3 = (1 + \eta)(1 + \xi) / 4 \\ N_4 = (1 - \eta)(1 + \xi) / 4 \end{cases} \quad (6)$$

The displacement function of any point in the element is shown in the following formula:

$$\begin{Bmatrix} u \\ v \end{Bmatrix} = \begin{Bmatrix} N_1 & 0 & N_2 & 0 & N_3 & 0 & N_4 & 0 \\ 0 & N_1 & 0 & N_2 & 0 & N_3 & 0 & N_4 \end{Bmatrix} \begin{Bmatrix} u_1 \\ v_1 \\ u_2 \\ v_2 \\ u_3 \\ v_3 \\ u_4 \\ v_4 \end{Bmatrix} \quad (7)$$

Where  $u_i$ ,  $v_i$  and  $n_i$  are the  $x$ ,  $y$  directions and interpolation functions of the four vertices respectively.

From the calculation results of the macro finite element model under three forging ratios of 15%, 22% and 35%, as shown in Figure 6, the displacement of four nodes of the target element is extracted. The target element is selected in the middle layer of the barrel, which is consistent with the sampling position of EBSD experimental specimen. Through the calculation Formula 7, the displacements of the four nodes are interpolated into the displacements of all

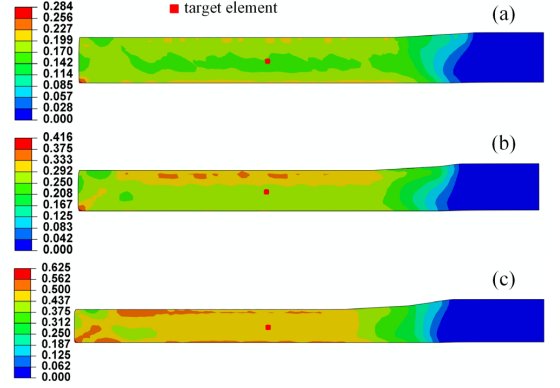


**Figure 6.** Equivalent plastic strain distribution of forged barrel with different forging ratios based on macro radial forging finite element model: (a) 15%; (b) 22%; (c) 35%.

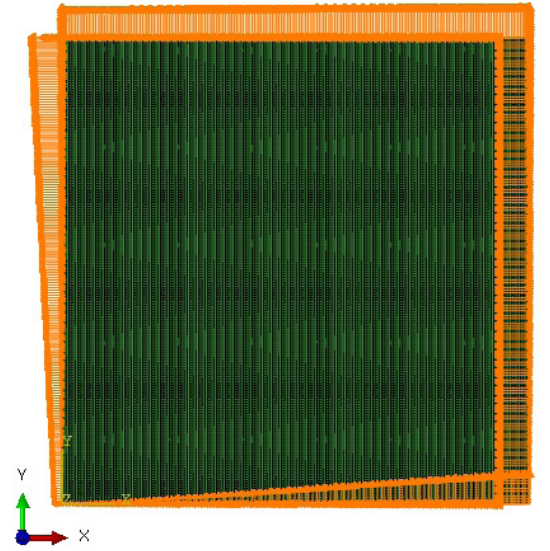


**Figure 7.** Node displacement boundary conditions of the CPFE model with 15% forging ratio.

nodes on each boundary of the meso polycrystalline finite element model. The boundary conditions of the 15% forging ratio CPFE model are shown in Figure 7.

## 4. Numerical Simulation Results and Analysis

### 4.1. Texture evolution

After forging, the deformation texture of barrel material 30SiMn2MoVA steel is represented by the pole figures.  $\{001\}$ ,  $\{111\}$  and  $\{101\}$  are the basic crystal planes of cubic crystal system. The pole figures of these three crystal planes can comprehensively reflect the distribution of grain crystal planes. The pole figures are shown in Figure 8 to Figure 10. The X in the pole figures shows the rolling direction. In this paper, it represents the axial direction of radial forged

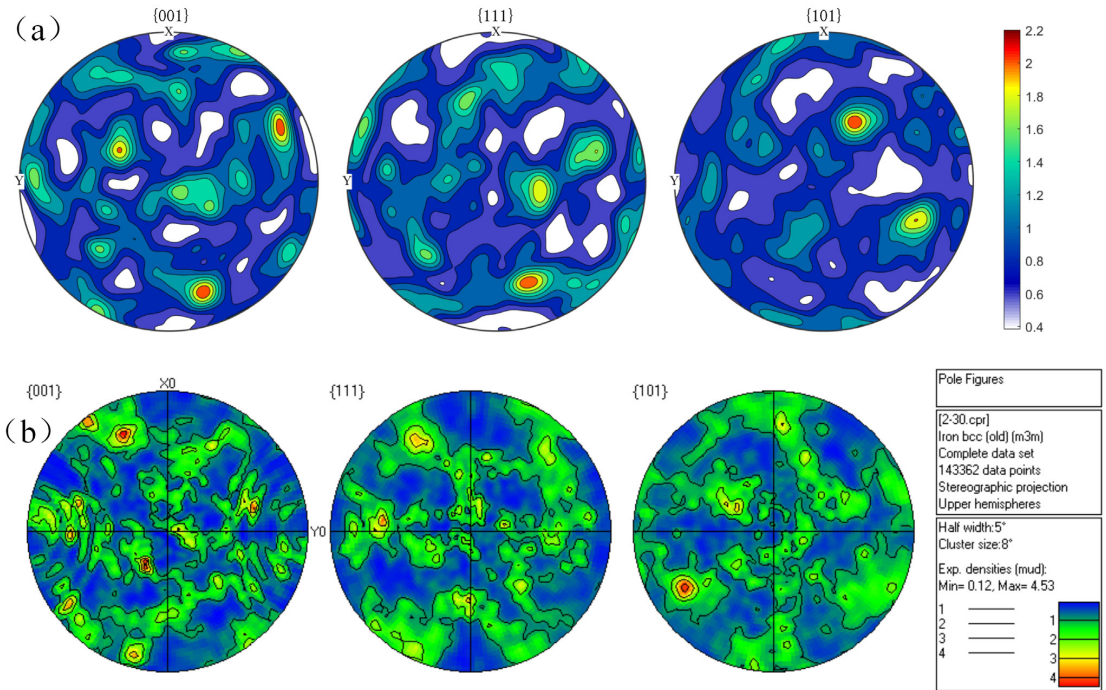


**Figure 8.** Grain orientation pole figures of forged 30SiMn2MoVA steel at 15% forging ratio: (a) simulation result; (b) EBSD test result.

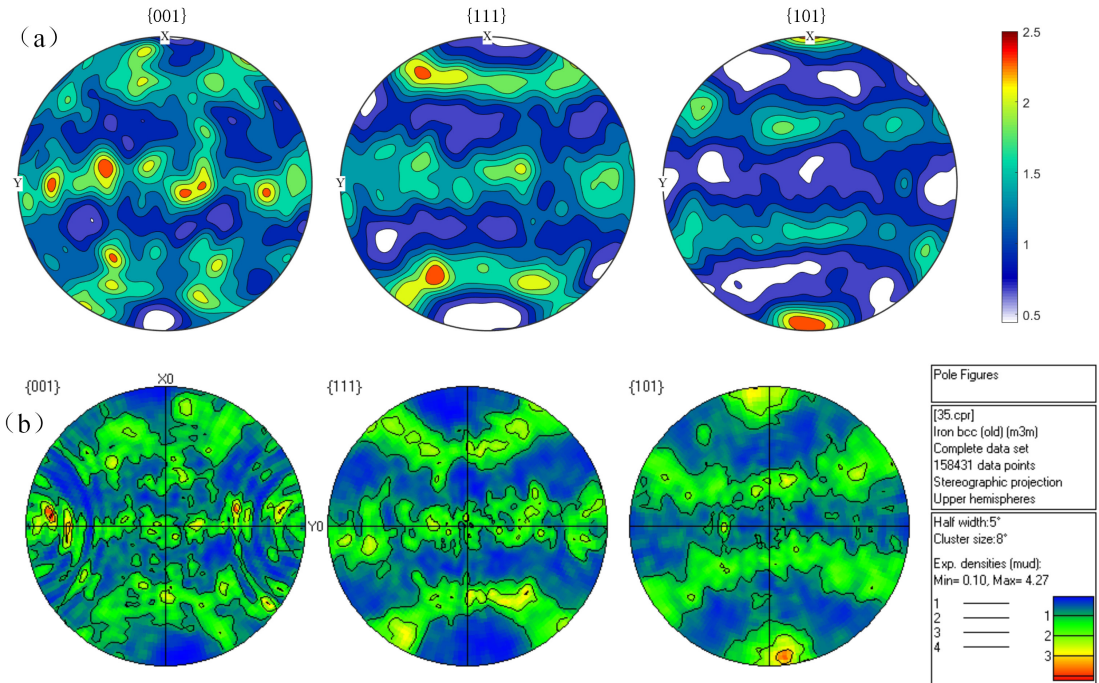


**Figure 9.** Grain orientation pole figure of forged 30SiMn2MoVA steel at 22% forging ratio: (a) simulation result; (b) EBSD test result.

barrel, and Y represents the transverse direction, namely, the circumferential direction of the forged barrel.

Figure 8 indicates the pole figures of the 15% forging ratio. The equivalent strain is 0.165 from Figure 6a. Due to its small deformation, there is no strong deformation texture. Its texture is relatively scattered and its intensity is weak.

Compared with the simulation and experimental results, it is relatively consistent in several places with strong texture intensity.

When the forging ratio is 22%, the equivalent strain of the forged tube becomes 0.273 from Figure 6b. Figure 9 shows the pole figures in the case of this plastic deformation.

The texture simulated in Figure 9a has been formed obvious texture. It is in good agreement with the EBSD results.

For the 35% forging ratio, the equivalent strain of the material is 0.463 in Figure 6c. Pole figures are shown in Figure 10. The value of the texture intensity is further improved. The simulated pole figures are roughly the same as the experiment.

The pole figure is the result of overlapping textures of various components in the deformed polycrystal, which is mainly the distribution of grain planes. It cannot reflect the change of grain orientation and show every texture component. In order to clearly identify the texture component of the forged tube under different forging ratios, this paper uses the orientation distribution function (ODF) to analyze the texture components of the polycrystalline model after deformation. Considering the crystal symmetry of BCC metal, it is generally selected  $\varphi_2=45^\circ$  ODF figure to analyze the deformation texture of 30SiMn2MoVA steel after radial forging. The CPFE calculation results and EBSD experimental results under different forging ratios are shown in Figure 11.

From Figure 10, the simulated ODF figures is consistent with the EBSD result except for texture intensity. In addition, the  $\{001\}\langle 110\rangle$  texture is observed and its intensity increased with the increase of deformation in the EBSD result. Nevertheless, this texture component is un conspicuous in the simulation, because the number of grains is small and the refinement effect of grains is not considered in the material model. With the increase of forging ratio,  $\alpha$ -fiber texture has been well developed, and the maximum value is concentrated in  $\{111\}\langle 110\rangle$  and  $\{110\}\langle 110\rangle$  texture. Meanwhile, the  $\{111\}\langle 110\rangle$  texture component in  $\gamma$ -fiber texture also increases with the increase of forging ratio. In

the cold rolling process, the typical deformation texture also includes the  $\{111\}\langle 112\rangle$  texture in the  $\gamma$ -fiber, however, this texture component does not appear in the cold radial forged steel tube.

#### 4.2. Inhomogeneous deformation of forged 30SiMn2MoVA gun barrel steel

In addition to being good at simulating deformation texture, CPFE can also intuitively show the changes of microstructure morphology. The evolution of microstructure morphology under different forging ratios is shown in Figure 12. The colors in the figure are only used to distinguish grains and do not contain other information. With the increase of deformation, the grains are obviously elongated along the axial direction. Generally, the grains will be broken and refined during the radial forging process. However, there is no the relevant attributes of grain refinement in the material model. Therefore, with the increase of forging ratio, the grain deformation in Figure 12 is intense and the phenomenon of grain breaking and refinement cannot occur.

Figure 13 shows the Mises stress distribution of polycrystalline model under different forging ratios. The stress of different grains varies greatly under the same deformation, as shown in the red and blue areas in the figure, and the Mises stress difference reaches about 1000MPa. If a large number grains are distributed at both ends of the whole stress region, which will lead to the increase of stress mutation points in the microstructure, which is lead to the initiation of microcracks<sup>34</sup>. This inhomogeneity will decrease as the amount of deformation increases. The number of grains in blue region and red region gradually decreases from Figure 13a-c. This is also confirmed by the

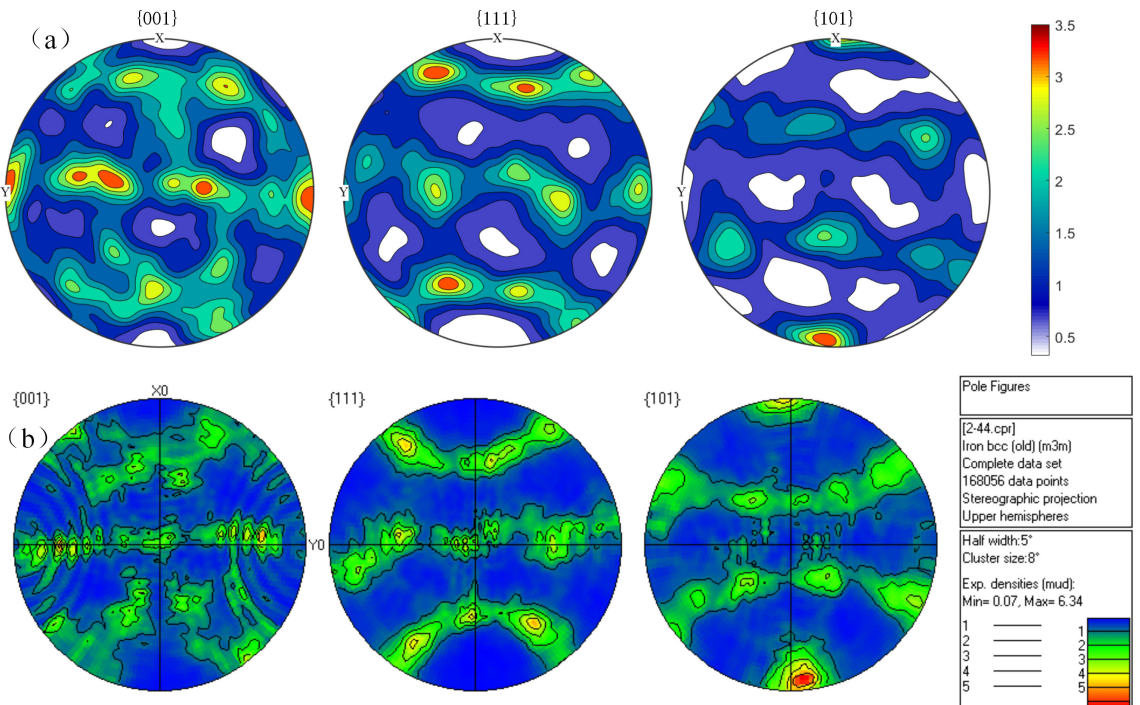
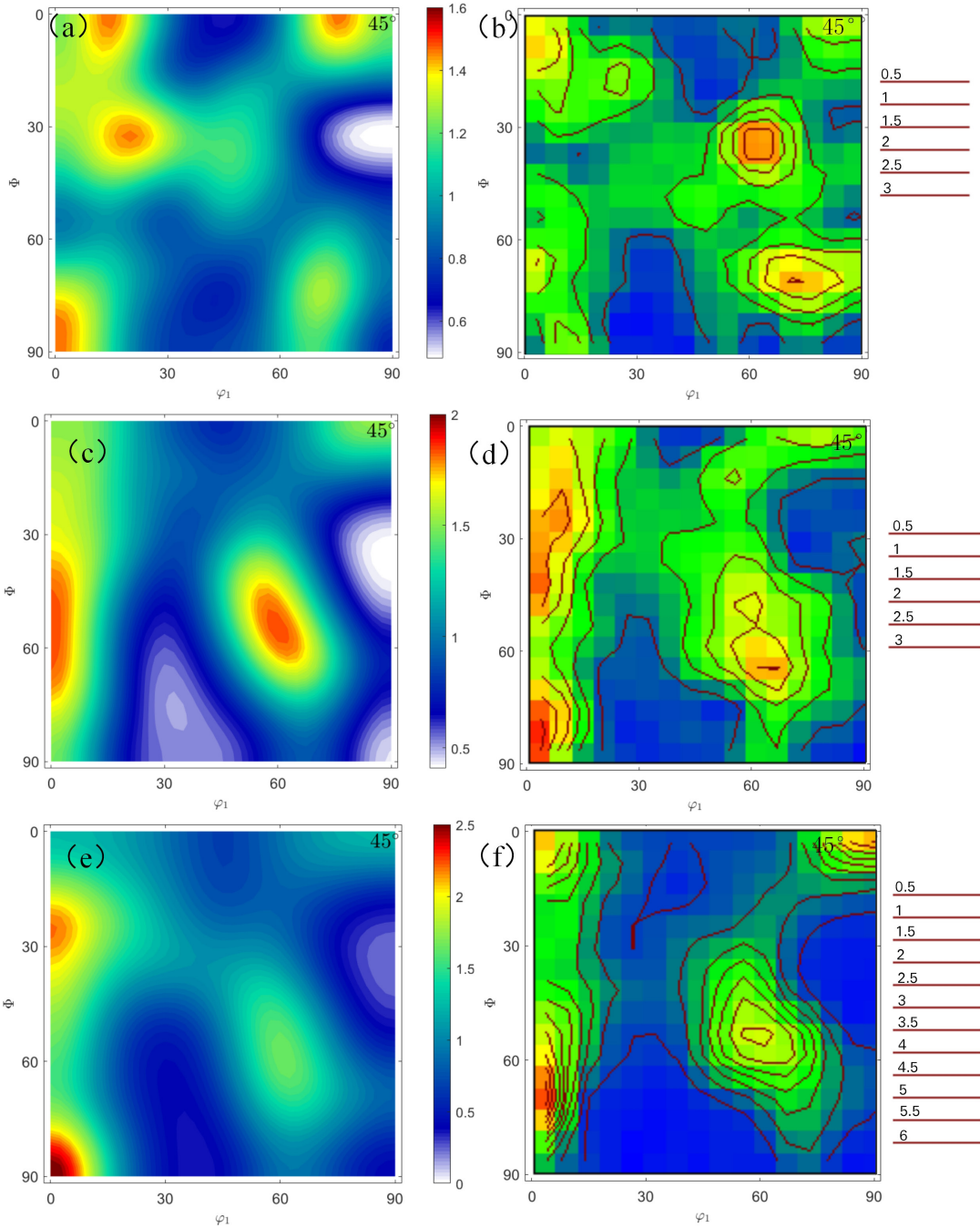


Figure 10 . Grain orientation pole figure of forged 30SiMn2MoVA steel at 35% forging ratio: (a) simulation result; (b) EBSD test result.



**Figure 11.**  $\phi_2=45^\circ$ ODF figure: (a) simulation result of 15% forging ratio; (b) EBSD experimental result of 15% forging ratio; (c) simulation result of 22% forging ratio; (d) EBSD experimental result of 22% forging ratio; (e) simulation result of 35% forging ratio; (f) EBSD experimental result of 35% forging ratio.

statistics of the number of grains in different stress intervals as shown in Figure 13d-f. The intracrystalline Mises stress of most grains is in the stress range of 600 to 1000 under large plastic deformation. The difference of grain orientation is the main reason for the anisotropy. Many grain orientations rotate parallel to the rolling direction with the increase of deformation, which makes the forged material show strong anisotropy.

Figure 14 shows the distribution of true strain distribution of CPFE model under different forging ratios. According to the simulation results of macro model, the equivalent plastic strain under 15% forging ratio is 0.165, 0.273 for the 22% forging ratio and 0.463 under the 35% forging ratio. From the distribution of true strain of grains, the true strain value is not close to the macro equivalent plastic strain. The severe deformation of grains (red area) occurs inside

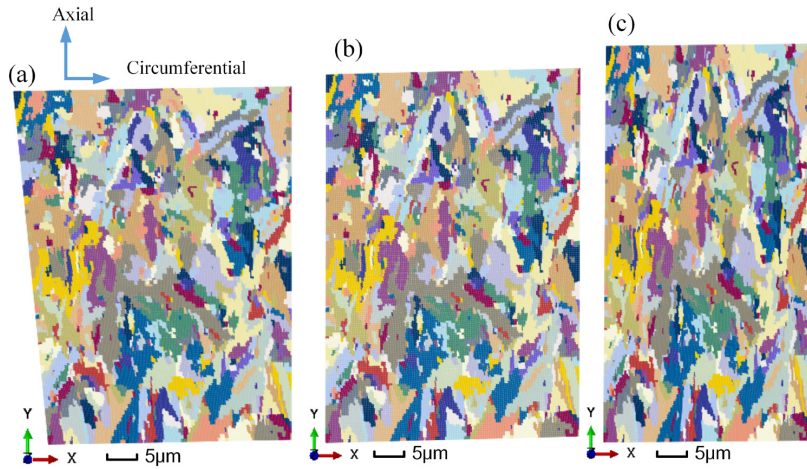


Figure 12 . Grain deformation of the forged 30SiMn2MoVA steel tube under the different forging ratio: (a) 15%; (b) 22%; (c) 35%.

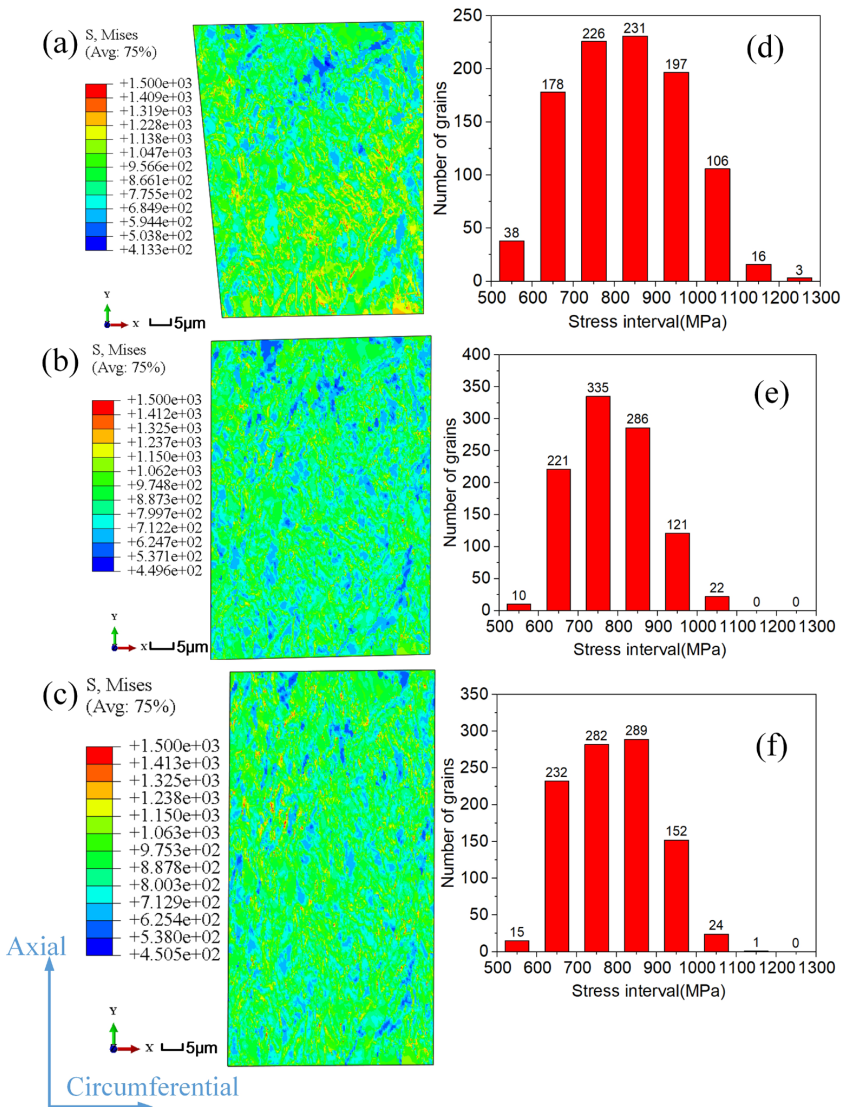
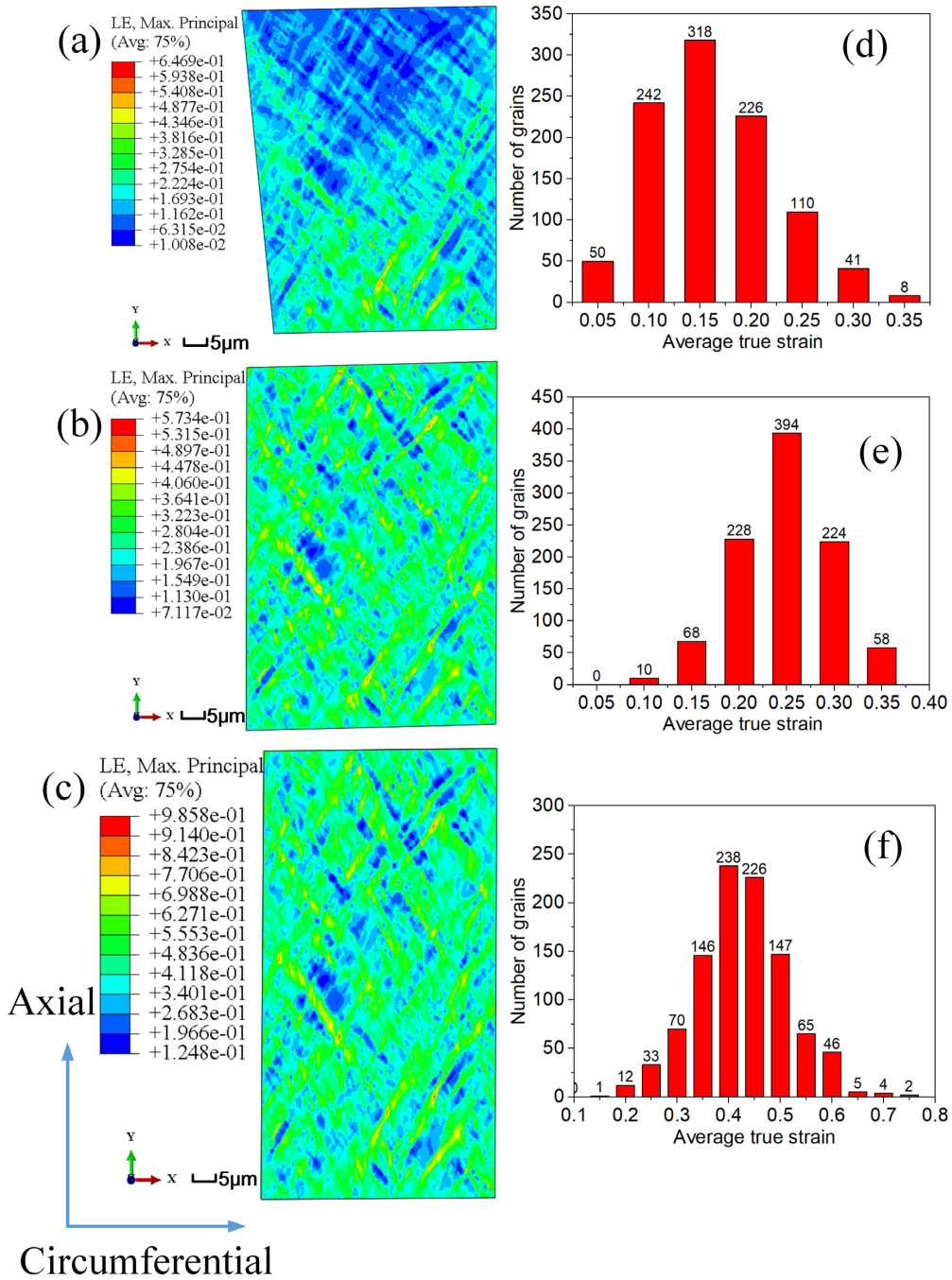


Figure 13. Mises stress distribution of the forged 30SiMn2MoVA steel tubes under the different forging ratio: (a)(d)15%; (b)(e)22%; (c)(f) 35%.



**Figure 14 .** True strain distribution of the forged 30SiMn2MoVA steel tubes under the different forging ratio: (a)(d)15%; (b)(e) 22%; (c) (f) 35%.

the grains. This severe deformation of grains has no clear relationship with their microstructure or grain shape, which is the result of coordinated deformation between grains. The inhomogeneous development of polycrystalline plastic deformation will also be affected by the action direction of the load. In the radial forging process, the tube extends along the axial direction. The direction at an angle of 45 degrees to the direction of elongation is the direction of maximum shear stress. In this direction, a slip channel conducive to

plastic deformation can be created. So, Figure 14a-c show that the plastic deformation in the polycrystal is distributed in a band at an angle of 45 degrees from the axial direction<sup>35</sup>. Figure 14d-f indicate that the number of grains in different strain intervals under three forging ratios. With the increase of forging ratio, the range of true strain is expanded. The maximum difference of true strain gradually changes from 0.3 (15% forging ratio) to 0.6(35% forging ratio), which reflects the degree of inhomogeneous deformation of polycrystal.

In the user material subroutine, the state variable (SDV) can be customized to output the variables needed to be observed. Figure 15a-c show the user defined cumulative shear strain  $\gamma$  of grains after forging. The plastic deformation mode of BCC metal is dislocation slip. The slip shear band formed by dislocation is the main reason for grain refinement. With the increase of forging ratio, the shear strain in the grain also gradually increases, as shown in Figure 15d-f. The

shear strain value in some grains is higher than that in the surrounding grains, and the number of grains with large shear strain gradually increases with the increase of deformation. Because the deformation coordination ability of large grains is weak, In the process of plastic deformation, there will be shear bands passing through the large grain, and the large grains will break and form small grains which is the reason for grain refinement by plastic deformation.

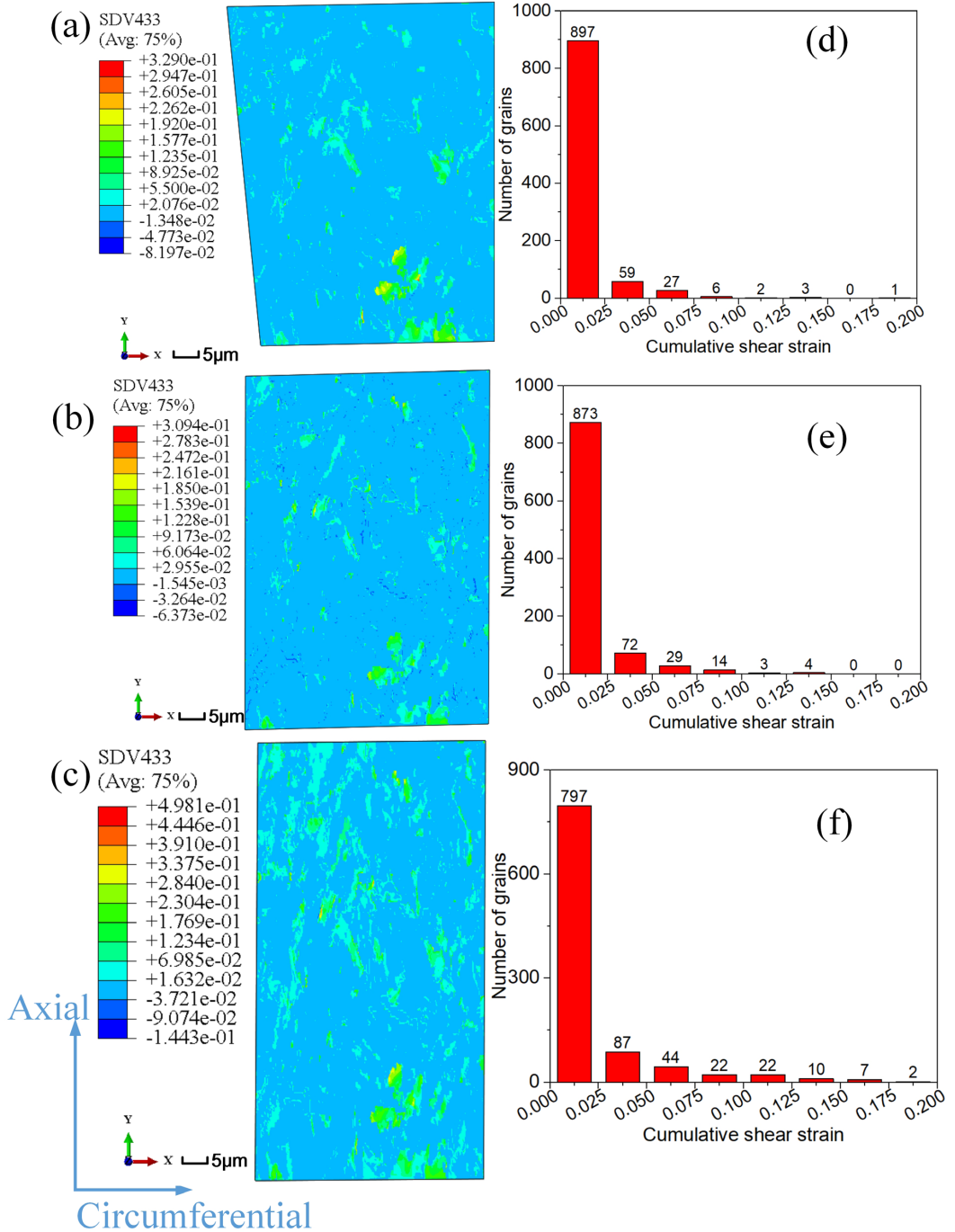


Figure 15 . Cumulative shear strain  $\gamma$  distribution of the forged 30SiMn2MoVA steel tubes under the different forging ratio :(a)(d) 15%; (b)(e) 22%; (c)(f) 35%.

## 5. Conclusions

In the present work, the deformation of 30SiMn2MoVA steel gun barrel with different forging ratios is simulated based on the CPFEM method. The main conclusions are as follows:

- (1) The main simulated deformation texture components are consistent with the experiment, which shows the availability of the CPFEM model. Through the CPFEM model, the texture of the radial forged gun barrel under arbitrary deformation can be predicted. Further, the anisotropy of the radial forged gun barrel can be calculated according to the texture components and volume fraction simulated by the CPFEM model, which can help to design the steel material to improve the mechanical properties of the steel gun barrel.
- (2) The stress and strain of the polycrystalline model under different forging ratios are analyzed. In the radial forging process of polycrystalline materials, the inhomogeneous deformation of grains is obvious. The distributions of stress and equivalent plastic strain in polycrystals are statistically Gaussian. This inhomogeneous deformation will intensify with the increase of the forging ratio.
- (3) For the total cumulative shear strain  $\gamma$  on all slip systems of grains, the analysis shows that with the increase of deformation, more and more large grains will have a large shear strain, which is due to the poor deformation coordination ability of large grains. In the process of radial forging, some shear bands will occur along large grains and it leads to the large grains breaking into small grains which is the reason for the grain refinement under plastic deformation.

## 6. Acknowledgments

The authors would like to acknowledge the Jiangsu Postdoctoral Research Funding Program, China (Grant No. 2021K040A).

## 7. References

1. Ghaei A, Movahhedy MR, Karimi Taheri A. Study of the effects of die geometry on deformation in the radial forging process. *J Mater Process Technol.* 2005;170(1-2):156-63. <http://dx.doi.org/10.1016/j.jmatprotec.2005.04.100>.
2. Yang Y, Fan L, Xu C, Dong X. Experimental study of mechanical properties of 30SiMn2MoVA steel gun barrel processed by cold radial forging. *J Press Vess-T ASME.* 2021;143(1):011501. <http://dx.doi.org/10.1115/1.4047654>.
3. Liang Y, Jiang S, Zhang Y, Zhao Y, Sun D, Zhao C. Deformation heterogeneity and texture evolution of NiTiFe shape memory alloy under uniaxial compression based on crystal plasticity finite element method. *J Mater Eng Perform.* 2017;26(6):2671-82. <http://dx.doi.org/10.1007/s11665-017-2678-7>.
4. Pi HC, Han JT, Xue YD, et al. Development on crystal plasticity finite modeling in metal forming. *J Mech Eng.* 2006;42(3):15-25. (in Chinese). <http://dx.doi.org/10.3901/JME.2006.03.015>.
5. Peirce D, Asaro RJ, Needleman A. An analysis of nonuniform and localized deformation in ductile single crystals. *Acta Metall.* 1982;30(6):1087-119. [http://dx.doi.org/10.1016/0001-6160\(82\)90005-0](http://dx.doi.org/10.1016/0001-6160(82)90005-0).
6. Harren SV, De'Ve H, Asaro RJ. Shear band formation in plane strain compression. *Acta Metall.* 1988;36(9):2435-80. [http://dx.doi.org/10.1016/0001-6160\(88\)90193-9](http://dx.doi.org/10.1016/0001-6160(88)90193-9).
7. Harren SV, Asaro RJ. Nonuniform deformations in polycrystals and aspects of the validity of the Taylor model. *J Mech Phys Solids.* 1989;37(2):191-232. [http://dx.doi.org/10.1016/0022-5096\(89\)90010-0](http://dx.doi.org/10.1016/0022-5096(89)90010-0).
8. Becker R. Analysis of texture evolution in channel die compression I: effects of grain interaction. *Acta Metall Mater.* 1991;39(6):1211-30. [http://dx.doi.org/10.1016/0956-7151\(91\)90209-J](http://dx.doi.org/10.1016/0956-7151(91)90209-J).
9. Becker R, Butler JF, Hu H, Lalli LA. Analysis of an aluminum single crystal with unstable initial orientation (001)[111] in channel die compression. *Metall Trans, A, Phys Metall Mater Sci.* 1991;22(1):45-58. <http://dx.doi.org/10.1007/BF03350948>.
10. Sachtleber M, Zhao Z, Raabe D. Experimental investigation of plastic grain interaction microstructure physics and metal forming. *Mater Sci Eng A.* 2002;336(1-2):81-7. [http://dx.doi.org/10.1016/S0921-5093\(01\)01974-8](http://dx.doi.org/10.1016/S0921-5093(01)01974-8).
11. Zhao Z, Ramesh M, Raabe D, Cuitiño AM, Radovitzky R. Investigation of three-dimensional aspects of grain-scale plastic surface deformation of an aluminum oligocrystal. *Int J Plast.* 2008;24(12):2278-97. <http://dx.doi.org/10.1016/j.ijplas.2008.01.002>.
12. Sarma GB, Radhakrishnan B, Zacharia T. Finite element simulations of cold deformation at the mesoscale. *Comput Mater Sci.* 1998;12(2):105-23. [http://dx.doi.org/10.1016/S0927-0256\(98\)00036-6](http://dx.doi.org/10.1016/S0927-0256(98)00036-6).
13. Beaudoin AJ Jr, Mecking H, Kocks UF. Development of localized orientation gradients in FCC polycrystals. *Philos Mag A Phys Condens Matter Struct Defects Mech Prop.* 1996;73(6):1503-17. <http://dx.doi.org/10.1080/01418619608242998>.
14. Zhao Z, Kuchnicki S, Radovitzky R, Cuitiño A. Influence of ingrain mesh resolution on the prediction of deformation textures in FCC polycrystals by crystal plasticity FEM. *Acta Mater.* 2007;55(7):2361-73. <http://dx.doi.org/10.1016/j.actamat.2006.11.035>.
15. Han TS, Dawson PR. A two-scale deformation model for polycrystalline solids using a strongly-coupled finite element methodology. *Comput Methods Appl Math.* 2007;196:2029-43. <http://dx.doi.org/10.1016/j.cma.2006.11.001>.
16. Zhang F, Bower AF, Mishra RK, Boyle KP. Numerical simulations of necking during tensile deformation of aluminum single crystals. *Int J Plast.* 2009;25(1):49-69. <http://dx.doi.org/10.1016/j.ijplas.2007.12.006>.
17. Bruzzi MS, McHugh PE, O'Rourke F, Linder T. Micromechanical modelling of the static and cyclic loading of an Al 2124-SiC MMC. *Int J Plast.* 2001;17(4):565-99. [http://dx.doi.org/10.1016/S0749-6419\(00\)00063-2](http://dx.doi.org/10.1016/S0749-6419(00)00063-2).
18. Park SJ, Han HN, Oh KH, Raabe D, Kim JK. Finite element simulation of grain interaction and orientation fragmentation during plastic deformation of BCC metals. *Mater Sci Forum.* 2002;408-412:371-6. <http://dx.doi.org/10.4028/www.scientific.net/MSF.408-412.371>.
19. Zhao Z, Roters F, Mao W, Raabe D. Introduction of a texture component crystal plasticity finite element method for anisotropy simulations. *Adv Eng Mater.* 2001;3(12):984-90. [http://dx.doi.org/10.1002/1527-2648\(200112\)3:12<984::AID-ADEM984>3.0.CO;2-L](http://dx.doi.org/10.1002/1527-2648(200112)3:12<984::AID-ADEM984>3.0.CO;2-L).
20. Melchior MA, Delannay L. A texture discretization technique adapted to polycrystalline aggregates with non-uniform grain size. *Comput Mater Sci.* 2006;37(4):557-64. <http://dx.doi.org/10.1016/j.commatsci.2005.12.002>.
21. Eisenlohr P, Roters F. Selecting a set of discrete orientations for accurate texture reconstruction. *Comput Mater Sci.* 2008;42(4):670-8. <http://dx.doi.org/10.1016/j.commatsci.2007.09.015>.
22. Beaudoin A, Mathur KK, Dawson PR, Johnson GC. Three-dimensional deformation process simulation with explicit use

- of polycrystal plasticity models. *Int J Plast.* 1993;9(7):833-60. [http://dx.doi.org/10.1016/0749-6419\(93\)90054-T](http://dx.doi.org/10.1016/0749-6419(93)90054-T).
23. Kalidindi SR, Schoenfeld SE. On the prediction of yield surfaces by the crystal plasticity models for FCC polycrystals. *Mater Sci Eng A.* 2000;293(1-2):120-9. [http://dx.doi.org/10.1016/S0921-5093\(00\)01048-0](http://dx.doi.org/10.1016/S0921-5093(00)01048-0).
  24. Chen YP, Lee WB, To S. Influence of initial texture on formability of aluminum sheet metal by crystal plasticity FE simulation. *J Mater Process Technol.* 2007;192-193:397-403. <http://dx.doi.org/10.1016/j.jmatprotec.2007.04.073>.
  25. Zhao Z, Radovitzky R, Cuitin˜o A. A study of surface roughening in FCC metals using direct numerical simulation. *Acta Mater.* 2004;52(20):5791-804. <http://dx.doi.org/10.1016/j.actamat.2004.08.037>.
  26. Roters F, Eisenlohr P, Hantcherli L, Tjahjanto DD, Bieler TR, Raabe D. Overview of constitutive laws, kinematics, homogenization and multiscale methods in crystal plasticity finite-element modeling: Theory, experiments, applications. *Acta Mater.* 2010;58(4):1152-211. <http://dx.doi.org/10.1016/j.actamat.2009.10.058>.
  27. Xu X, Fan LX, Wang YP, Dong XB. Trans-scale polycrystalline finite element simulation of radial forging process for barrel and prediction of texture. *Acta Armamentarii.* 2016;37(7):1180-6. (in Chinese). <https://doi.org/10.3969/j.issn.1000-1093.2016.07.004>.
  28. Huang Y. A user-material subroutine incorporating single crystal plasticity in the ABAQUS finite element program. Cambridge: Division of Engineering and Applied Sciences, Harvard University; 1991. p. 1-21. (Mech Report; 178).
  29. Kovač M, Cizelj L. Modeling elasto-plastic behavior of polycrystalline grain structure of steels at mesoscopic level. *Nucl Eng Des.* 2005;235(17-19):1939-50. <http://dx.doi.org/10.1016/j.nucengdes.2005.05.009>.
  30. Mainprice F, Bachmann R, Hielscher H, Schaeben H. Descriptive tools for the analysis of texture projects with large datasets using MTEX: strength, symmetry and components. *Geol Soc Lond Spec Publ.* 2015;409(1):251-71. <http://dx.doi.org/10.1144/SP409.8>.
  31. Latypov MI, Shin S, De Cooman BC, Kim HS. Micromechanical finite element analysis of strain partitioning in multiphase medium manganese TWIP+TRIP steel. *Acta Mater.* 2016;108:219-28. <http://dx.doi.org/10.1016/j.actamat.2016.02.001>.
  32. Nicolò G, Earp P, Cocks ACF, et al. Characterization of slip and twin activity using digital image correlation and crystal plasticity finite element simulation: application to orthorhombic  $\alpha$ -uranium. *J Mech Phys Solids.* 2019;135:103800. <http://dx.doi.org/10.1016/j.jmps.2019.103800>.
  33. Nicolò G. ebsd2abaqusEuler [Internet]. 2020 [cited 2020 Oct 5]. Available from: <https://github.com/ngrilli/ebsd2abaqusEuler>
  34. Li J, Li X, Cheng J, et al. Trans-scale simulation of polycrystalline material components. *J Mech Eng.* 2011;47(10):43-51. (in Chinese). <http://dx.doi.org/10.3901/JME.2011.10.043>.
  35. Zhang K. Deformation, stress inhomogeneity and macroscopic response of polycrystals. *Chin J Theor Appl Mech.* 2004;36(6):714-23. (in Chinese). <https://doi.org/10.3901/JME.2011.10.043>.